Chemical Science

ROYAL SOCIETY OF CHEMISTRY

EDGE ARTICLE

View Article Online
View Journal

Check for updates

Cite this: DOI: 10.1039/d6sc01364c

All publication charges for this article have been paid for by the Royal Society of Chemistry

Confining ultrasmall Au nanoclusters in an ionic Ir(III)-based cage for selective photoreduction

Zhuolin Shi,[a] Fengyang Yu,[b] Jinguo Wu,[a] Yongai Yu,*[a] Hanshu Li,[a] Xing Zhao,[a] Rong Zhang,[a] Wenjing Jiang,[c] Yiwei Liu,[a] Jianwei Wei,[d] Xuezhao Li *[a] and Cheng He[a]

Balancing activity and stability in metal nanoclusters (NCs) for efficient catalysis remains challenging, particularly in tuning their surrounding microenvironment to control selectivity. Here, we report ultrasmall Au nanoclusters (0.73 ± 0.14 nm) confined within a photoactive dinuclear Ir(III)-based ionic cage, synergistically coupling spatial confinement with electronic cooperativity for selective photoreduction. The ionic cage enables controlled synthesis of ultrasmall Au–NCs, ensures long-term stability (>6 months) and facilitates photoinduced electron transfer (PET) from Ir(III) photosensitizers to Au active sites. This multi-function design drives complete nitrobenzene-to-azobenzene conversion with >98% selectivity under visible light (450 nm) at room temperature, avoiding aniline byproducts. *Operando* spectroscopy, kinetic studies, and DFT calculations reveal that substrate-sieving at cage windows directs the stepwise reduction pathway *via* azoxybenzene intermediates. The demonstrated integration of photoinduced electronic and steric microenvironment control of cage-encapsulated NC-based composites establishes a promising strategy for developing nanocatalysts with exceptional selectivity steering capability.

Received 15th February 2026
Accepted 12th April 2026

DOI: 10.1039/d6sc01364c

rsc.li/chemical-science

Open Access Article. Published on 23 April 2026. Downloaded on 6/10/2026 5:52:33 AM. This article is licensed under a Creative Commons Attribution-NonCommercial 3.0 Unported Licence.

Introduction

Metal nanoclusters (NCs)—typically less than 2 nm in size—have garnered significant attention due to their molecule-like electronic structures and high surface-area-to-volume ratios, which collectively endow them with outstanding catalytic activity.[1,2] However, their inherently high surface energy renders them thermodynamically unstable, often leading to aggregation into larger particles.[3] To address this, effective stabilization strategies employing organic ligands, polymers, or porous frameworks (*e.g.*, MOFs, COFs) have been explored.[4–8] Nevertheless, these approaches may hinder efficient substrate-catalyst interactions, introduce diffusion limitations, and importantly lack precise control over the microenvironment around the active sites, which limits achievable selectivity.[9] Therefore, the challenge remains to design a confined yet accessible microenvironment that not only stabilizes ultrasmall NCs but also exerts precise control over substrate access to govern catalytic selectivity.[10]

In natural systems, high catalytic activity and selectivity often arise from spatially confined microenvironments that regulate substrate access and reaction pathways, as exemplified by enzyme active-site pockets.[11,12] Spatial confinement within well-defined nanocavities represents a powerful strategy for enhancing catalytic selectivity and steering reaction pathways.[13–15] In this context, molecular cages (MCs) stand out as promising hosts for NCs. Their well-defined, processable cavities allow for precise spatial confinement of substrates and fine-tuning of the catalytic microenvironment.[16–29] Compared to extended porous frameworks, MCs offer modular and atomically precise control over structure and functionality, which enables simultaneous protection of NCs and substrate accessibility to catalytic sites.[30–34] Their capacity to organize multiple components within a confined volume mirrors the architecture of enzyme active pockets, facilitating cascade reactions and suppressing side pathways.[35,36] Despite these advantages, most reported nanocatalysts based on purely organic molecular cages rely on flexible scaffolds that often lack sufficient structural rigidity and are prone to collapsing in solution.[37–39] In addition, the integration of photoactive components into molecular cages to enable cooperative, light-driven catalysis with encapsulated metal NCs remains underexplored.[40,41]

In this study, we report an advanced catalytic platform comprising ultrasmall Au nanoclusters (Au–NCs, 0.73 ± 0.14

[a]Central Hospital of Dalian University of Technology, School of Chemistry, School of Chemical Engineering, Dalian University of Technology, Dalian 116024, China. E-mail: xuezhaoli@dlut.edu.cn; yuyongai@dlut.edu.cn

[b]College of Chemistry, Xinjiang University, Xinjiang, 830046, China

[c]Fujian Science & Technology Innovation Laboratory for Optoelectronic Information of China, Fuzhou, Fujian 350108, China

[d]Hebei Technology Innovation Center for Energy Conversion Materials and Devices, College of Chemistry and Materials Science, Hebei Normal University, Shijiazhuang 050024, China

© 2026 The Author(s). Published by the Royal Society of Chemistry

Open Access Article. Published on 23 April 2026. Downloaded on 6/10/2026 5:52:33 AM. This article is licensed under a Creative Commons Attribution-NonCommercial 3.0 Unported Licence.

nm) confined within a photoactive dinuclear Ir(III)-based ionic cage. The Ir(III) cage not only directs the formation of ultrasmall Au–NCs but also serves as a built-in photosensitizer, enabling efficient PET to the surface of Au–NCs. This synergistic design enables complete photoreduction of nitrobenzene to azobenzene *via* azoxybenzene intermediates, achieving >98% selectivity under 450 nm light irradiation at room temperature, while effectively suppressing over-reduction to aniline. Mechanistic insights derived from kinetic analyses, *operando* spectroscopy, and DFT calculations comprehensively elucidate the origins of the system's high selectivity: size-exclusion effects at cage windows and the photoinduced formation of an electron-rich Au–NCs surface. Our results demonstrate the potential of integrating spatial confinement and photoactive functionality within a single cage skeleton to confine ultrasmall nanoclusters, creating advanced catalytic systems with specific selectivity.

Results and discussion

Design, synthesis, and characterization of the ionic dinuclear Ir(III)-based cage

We previously reported a pair of homochiral dinuclear Ir(III)-based cages, Δ_2R_6-**Hi** and Λ_2S_6-**Hi**, constructed from three enantiopure *trans*-1,2-diaminocyclohexane (DACH, RR/SS-form) spacers and two fac-Ir(ppy)$_3$ (ppy = 2-phenylpyridine) vertices in either Δ- or Λ-configurations, connected *via* imine linkages (Fig. S1–S3).[42] Upon reduction of the imine bonds and subsequent acidification of the resulting neutral amine-linked cage, we envisioned that the resulting ionic Ir(III)-based cage could serve as an ideal host for ultrasmall NCs, owing to several distinct advantages:

(1) The resulting cationic cage (+6) is highly water-soluble and stable. It can trap anionic metal precursors through electrostatic interactions while simultaneously preventing aggregation of the encapsulated NCs *via* coulombic repulsion—thus acting as a "cationic armor".

(2) The rigid fac-Ir(ppy)$_3$ vertices define a confined internal cavity suitable for size-controlled NC growth. Meanwhile, their photoactive nature enables potential synergy with encapsulated NCs in photocatalytic processes.[43]

(3) Crucially, the open cage windows are expected to allow for substrate diffusion and modulate interactions between the NC surface and incoming molecules, providing a spatially confined microenvironment conducive to selective transformations.

To this end, we selected the Δ_2R_6-**Hp** cage as a model system. As illustrated in Fig. 1a, its synthesis involved two steps: (i) reduction of Δ_2R_6-**Hi** with $NaBH_4$ to obtain the amine-linked neutral cage Δ_2R_6-**Ha**, and (ii) subsequent protonation with dilute HCl to afford the final ionic cage Δ_2R_6-**Hp**. Both Δ_2R_6-**Ha**

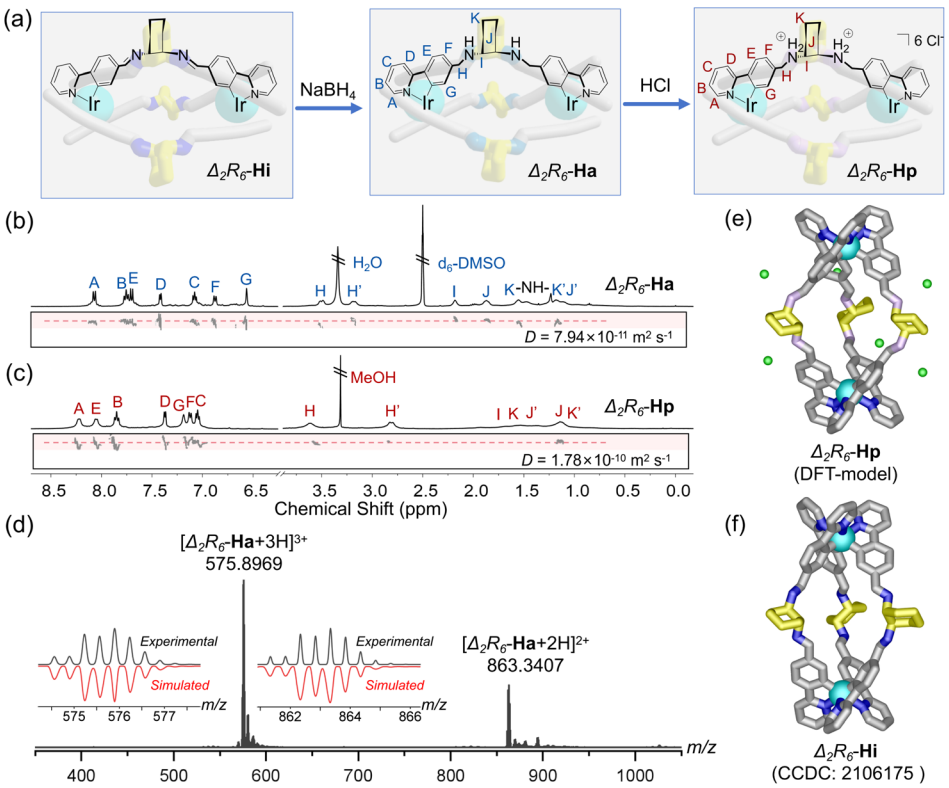

Fig. 1 (a) Stepwise formation of the ionic Δ_2R_6-**Hp** by HCl-acidifying of the neutral amine-linked Δ_2R_6-**Ha** from the imine-linked Δ_2R_6-**Hi**. (b) Partial ^{1}H NMR and DOSY spectra of Δ_2R_6-**Ha** (400 MHz, DMSO-d_6). (c) Partial ^{1}H NMR and DOSY spectra of Δ_2R_6-**Hp** (400 MHz, D_2O). (d) HR-Q-TOF-MS spectra of Δ_2R_6-**Ha**. Magnified areas show the measured and calculated isotopic patterns. (e) The DFT structure model of Δ_2R_6-**Hp**. (f) Crystal structures of Δ_2R_6-**Hi**. Color code: C atom: grey, yellow (for DACH); N atom: blue, pink (for DACH in Δ_2R_6-**Hp**); Ir atom: cyan, Cl atom: green. Hydrogen atoms and solvate molecules have been omitted for clarity.

© 2026 The Author(s). Published by the Royal Society of Chemistry

Open Access Article. Published on 23 April 2026. Downloaded on 6/10/2026 5:52:33 AM. This article is licensed under a Creative Commons Attribution-NonCommercial 3.0 Unported Licence.

and Δ_2R_6-**Hp** were isolated in good yields and fully characterized by nuclear magnetic resonance (NMR) and high-resolution quadrupole time-of-flight mass spectrometry (HR-Q-TOF-MS) (Fig. S4–S33). In particular, the characteristic imine proton signals of Δ_2R_6-**Hi** disappeared, and new signals corresponding to NH (1.47 ppm) and methylene protons (3.18 and 3.50 ppm) appeared in the ^{1}H NMR spectrum of Δ_2R_6-**Ha** (Fig. 1b). Moreover, diffusion-ordered NMR spectroscopy (^{1}H DOSY) showed a single diffusion band ($D = 7.94 \times 10^{-11}$ m^2 s^{-1}), consistent with a single discrete species. Correspondingly, HR-Q-TOF-MS analysis of Δ_2R_6-**Ha** revealed two dominant peaks at m/z = 863.3407 ($[M + 2H]^{2+}$, calc. 863.3415) and m/z = 575.8969 ($[M + 3H]^{3+}$, calc. 575.8968), collectively confirming the complete conversion of imines to amines (Fig. 1d). Subsequent protonation of Δ_2R_6-**Ha** with dilute HCl (~0.12 M, 12 h, r.t.) afforded the water-soluble ionic cage Δ_2R_6-**Hp**. In D_2O, ^{1}H NMR showed a single set of well-resolved signals, and ^{1}H DOSY NMR displayed a consistent diffusion coefficient ($D = 1.78 \times 10^{-10}$ m^2 s^{-1}) (Fig. 1c), indicating the formation of a uniform species. HR-Q-TOF-MS confirmed the intact $[M - 4H - 6Cl]^{2+}$ and $[M - 3H - 6Cl]^{3+}$ species (Fig. S19). Furthermore, Δ_2R_6-**Hp** exhibits excellent aqueous solubility and thermal stability (Fig. S34), with no significant changes in the NMR spectra after heating at 90 °C for 48 h. Importantly, the protonation process was reversible: treatment with excess NaOH regenerated Δ_2R_6-**Ha** as a yellow precipitate, confirming that it is acid/base-switchable without compromising structural integrity.

Crystallization attempts for Δ_2R_6-**Hp** were unsuccessful, thus density functional theory (DFT) calculations were employed to model its structural properties. Notably, in contrast to many purely organic amine-linked cages that collapse after imine reduction due to backbone flexibility, the rigid Ir(III) modules in Δ_2R_6-**Hp** preserved the integrity of the cavity architecture.[42] As illustrated in Fig. 1e, three RR-DACH spacers bridge two fac-Ir(ppy)$_3$ vertices, both adopting the same Δ-configuration. The protonated –NH_2^+- groups introduce electrostatic repulsion between them, which expands the transverse dimension of the cavity, resulting in a more open and near-spherical geometry compared to the imine-linked Δ_2R_6-**Hi** (Fig. 1f).[42] Correspondingly, the calculated average N···N distance increased to approximately 8.8 Å (from 8.1 Å), while the Ir···Ir distance decreased to 12.7 Å (from 13.3 Å). These robust and tunable structural features, combined with the enlarged internal cavity of Δ_2R_6-**Hp**, render it a promising platform for the encapsulation of ultrasmall Au–NCs.

Encapsulation of Au–NCs in the ionic Ir(III)-based cage. Encapsulation of ultrasmall Au nanoclusters (Au–NCs) within the molecular cage Δ_2R_6-**Hp** was achieved *via* a stepwise procedure involving electrostatic complexation followed by *in situ* chemical reduction (Fig. 2a).[36] Specifically, $AuCl_4^-$ anions

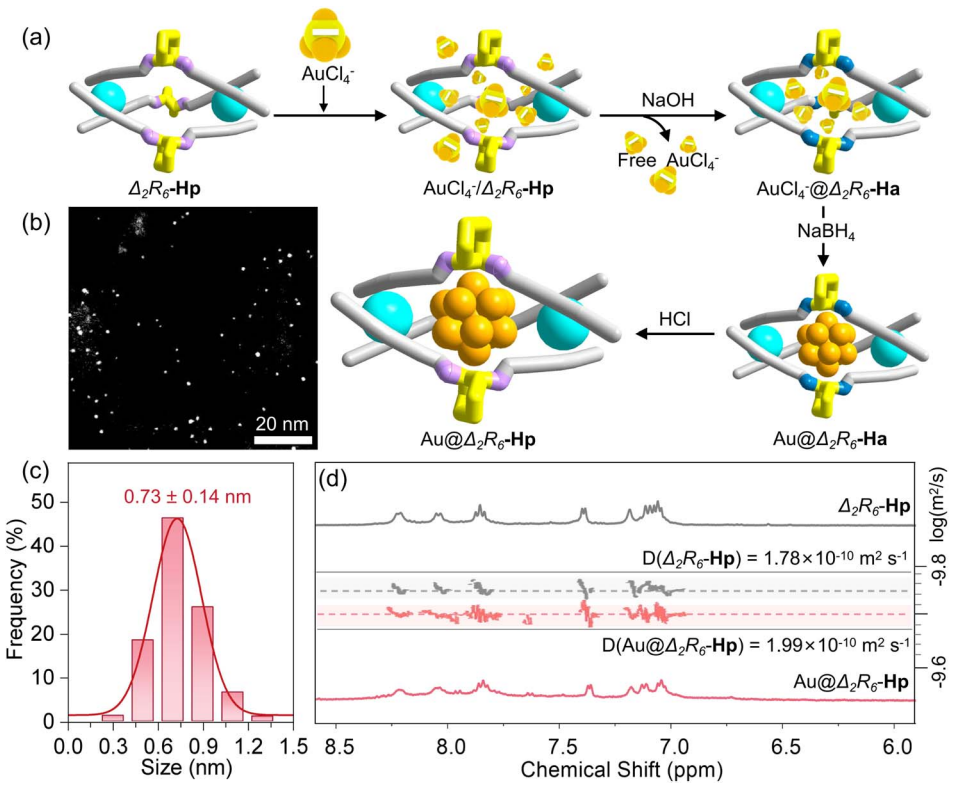

Fig. 2 (a) Schematic illustration of the stepwise synthesis of Au@Δ_2R_6-**Hp** involving: (i) electrostatic complexation encapsulates $AuCl_4^-$ inclusion into the Δ_2R_6-**Hp** cavity; (ii) base treatment isolates the precipitate of $AuCl_4^-$@Δ_2R_6-**Ha** to remove unencapsulated $AuCl_4^-$; (iii) *in situ* $NaBH_4$ reduction of $AuCl_4^-$@Δ_2R_6-**Ha**; (iv) protonation of Au@Δ_2R_6-**Ha** to yield Au@Δ_2R_6-**Hp**. (b and c) Spherical aberration HAADF-STEM image and corresponding statistical size distribution histogram of encapsulated Au–NCs in Δ_2R_6-**Hp**. (d) Partial ^{1}H NMR and DOSY spectra (400 MHz, D_2O) of Δ_2R_6-**Hp** (gray) and Au@Δ_2R_6-**Hp** (pink).

© 2026 The Author(s). Published by the Royal Society of Chemistry

Open Access Article. Published on 23 April 2026. Downloaded on 6/10/2026 5:52:33 AM. This article is licensed under a Creative Commons Attribution-NonCommercial 3.0 Unported Licence.

were introduced into an aqueous solution of Δ_2R_6-**Hp**, where the positively charged cages, individually dispersed due to electrostatic repulsion, attracted and trapped the negatively charged gold precursors. Zeta potential measurements revealed a decrease in surface charge from +34.6 to +22.3 mV upon complexation, confirming successful electrostatic loading (Fig. S44).[36] The ^{1}H NMR titration of Δ_2R_6-**Hp** with $AuCl_4^-$ revealed obvious chemical shift changes in aromatic and methylene protons, coupled with pronounced line broadening, demonstrating strong electrostatic binding of the anions within the cage pockets (Fig. S45).[44] Subsequently, neutralization of the $AuCl_4^-/\Delta_2R_6$-**Hp** mixture generated a precipitate of $AuCl_4^-$@-Δ_2R_6-**Ha**, from which free $AuCl_4^-$ ions were removed. The encapsulated Au–NCs were then formed *via in situ* reduction using dropwise addition of $NaBH_4$ (yielding Au@Δ_2R_6-**Ha**). The secondary amine groups in the cage were further protonated to yield Au@Δ_2R_6-**Hp**—a water-soluble and stable nanocluster composite. X-ray photoelectron spectroscopy (XPS) displayed the peaks at 87.4 and 83.8 eV (Au $4f_{5/2}$ and $4f_{7/2}$), confirming the dominance of metallic Au^0 species (Fig. S46).[1] The morphology of Au@Δ_2R_6-**Hp** was visualized by aberration corrected high-angle annular dark-field scanning transmission electron microscopy (HAADF-STEM). The Au existed as ultrafine clusters with an average size of 0.73 ± 0.14 nm and a narrow size distribution (Fig. 2b and c), and such a small size distribution matches well with the cavity size of Δ_2R_6-**Hp**.[30–34,36] Elemental mapping of Ir and Au further confirmed that the Au–NCs are spatially associated with the Ir-based cages, with no evidence of isolated Au aggregates (Fig. S47). Inductively coupled plasma optical emission spectrometry (ICP-OES) revealed a gold loading of 25.9 wt% (Fig. S48). ^{1}H DOSY NMR experiments further showed that the diffusion coefficient of Au@Δ_2R_6-**Hp** ($D = 1.99 \times 10^{-10}$ m^2 s^{-1}) closely resembled that of the empty cage ($D = 1.78 \times 10^{-10}$ m^2 s^{-1}). This result indicated that Au@Δ_2R_6-**Hp** diffuses as a single cage-sized entity in solution, thereby excluding the possibility that the encapsulated NCs are stabilized by multiple cages (Fig. 2d).[36] Additionally, the absence of diffraction peaks from metallic Au in PXRD patterns and the lack of surface plasmon resonance (SPR) features in the UV-vis absorption spectra confirmed the ultrasmall and non-aggregated nature of the clusters (Fig. S49 and S50).[30,33,45,46]

The cationic skeleton of Δ_2R_6-**Hp** endows exceptional stability to the encapsulated Au–NCs in aqueous media *via* electrostatic repulsion, maintaining dispersion integrity without aggregation for over six months, as evidenced by consistent UV-vis spectra and HAADF-STEM imaging (Fig. S51). Importantly, employing Λ_2S_6-**Hp** as an alternative host also produced ultrasmall Au–NCs with comparable dimensions (Fig. S53), demonstrating the general applicability of these metallohelical cages as templates for nanocluster synthesis. In contrast, control experiments using Δ_2R_6-**Ha**, which lacks electrostatic trapping and stabilization abilities, yielded significantly larger nanoparticles (Au/Δ_2R_6-**Ha**, average size: 2.36 ± 0.61 nm, Fig. S54), indicating that the particles formed outside the cage cavity and were merely surrounded by cages. The PXRD pattern of Au/Δ_2R_6-**Ha** showed multiple diffraction peaks in the 30–70° range, consistent with the presence of crystalline Au nanoparticles (Fig. S55).[33] These results highlight the critical role of electrostatic interactions in achieving both ultrasmall cluster size and long-term stability.

Reaction development of photoreduction. Azobenzene (**AB**), a key intermediate for dyes and pharmaceuticals, is typically synthesized by reducing nitrobenzene (**NB**).[47,48] However, precise chemoselectivity control in this process remains

Table 1 Catalytic performance for the reduction of NB[a]

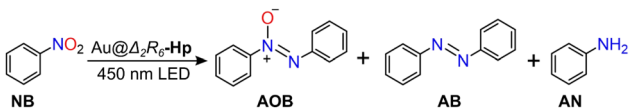

Entry	Variation from the "standard conditions"	Conversion/%	Seletivity/%		
			AOB	AB	AN
1	None	100	—	98	2
2	Au@Λ_2S_6-**Hp**	100	—	98	2
3	No catalyst	5.5	5.5	—	—
4	No light	0	—	—	—
5	Δ_2R_6-**Hp**	33	33	—	—
6	$AuCl_4^-/\Delta_2R_6$-**Hp**	20	88	12	—
7	Au/Δ_2R_6-**Ha**	100	57	29	14
8	EtOH replaces IPA	0	—	—	—
9	None (48 h)	100	—	98	2
10	None (72 h)	100	—	95	5
11	None (after five cycles)	100	17	83	—

[a] Reaction conditions: Au@Δ_2R_6-**Hp** (1 mol%), 0.1 mmol of **NB**, 2 mL of IPA, 0.3 M of NaOH, room temperature, Ar atmosphere, 450 nm LED, reaction time of 24 h.

© 2026 The Author(s). Published by the Royal Society of Chemistry

Open Access Article. Published on 23 April 2026. Downloaded on 6/10/2026 5:52:33 AM. This article is licensed under a Creative Commons Attribution-NonCommercial 3.0 Unported Licence.

challenging due to competing pathways involving intermediates that favor byproducts like azoxybenzene (**AOB**) and aniline (**AN**).[49–51] We hypothesized that the unique structural design of Au@Δ_2R_6-**Hp**, in which ultrasmall Au–NCs are encapsulated by an ionic Ir(III)-based cage, provides a confined microenvironment that enable controlled substrate access and substrate-sieving functionality. These structural features position Au@Δ_2R_6-**Hp** as an ideal platform for controlling multistep selective **NB** reductions under visible-light-driven photocatalysis. Encouragingly, under optimized conditions, complete **NB** conversion with an outstanding 98% selectivity toward **AB** was achieved (Table 1, entries 1 and 2). Control experiments confirmed that this selectivity and activity were attributable to the synergistic interplay between the ultrasmall Au–NCs and the photoactive cage. In the absence of either the catalyst or light, negligible product formation was observed (Table 1, entries 3 and 4). Replacing Au@Δ_2R_6-**Hp** with Δ_2R_6-**Hp** resulted in only 33% **NB** conversion (Table 1, entry 5), demonstrating that the cage alone is insufficient to promote the reduction of **AOB** to **AB**. Control experiments using a mixture of Δ_2R_6-**Hp** and $HAuCl_4$ resulted in limited conversion (20%), yielding **AOB** and **AB** in 88% and 12%, respectively (Table 1, entry 6). Similarly, the large-sized Au/Δ_2R_6-**Ha** system showed poor chemoselectivity, yielding 57% **AOB** and only 29% **AB** (Table 1, entry 7). Collectively, these results highlight the superior catalytic selectivity of the cage-encapsulated ultrasmall Au–NCs platform in the visible light-driven photocatalytic reduction of **NB** to **AB**. The proton donor properties of the solvent were also found to play a crucial role. Isopropanol (IPA) proved essential in donating protons during the reduction, while the addition of NaOH enhanced hydrogen abstraction from IPA, thereby accelerating the reaction rate.[33,49,50] In contrast, ethanol (EtOH), a weaker proton donor, failed to promote the reaction, showing negligible activity (Table 1, entry 8). Remarkably, the Au@Δ_2R_6-**Hp** catalyst maintained high selectivity (98% and 95%) toward **AB** even after prolonged reaction times of 48 and 72 h, respectively (Table 1, entries 9 and 10). In addition, the catalyst retained high activity over five consecutive cycles, with a slight decrease in selectivity (Table 1, entry 11). PXRD analysis after five catalytic cycles revealed no diffraction peaks attributable to large, crystalline Au nanoparticles, indicating that macroscopic aggregation does not occur during catalysis (Fig. S57).[33] Consistently, HAADF-STEM images collected after the catalytic cycles revealed a slight increase in the size of the Au–NCs (~0.89 nm, Fig. S58), potentially associated with the minor loss in selectivity. Removal of the catalyst by filtration after 4 h completely suppressed further conversion under continued irradiation (Fig. S59). ICP-OES analysis of the supernatant following catalyst removal showed negligible Au leaching, demonstrating the good stability of the encapsulated Au–NCs (Fig. S60).

The general applicability of Au@Δ_2R_6-**Hp** was evaluated in the selective photocatalytic coupling of various nitroarenes bearing diverse functional groups (Table 2). Halogenated nitroarenes, including F-, Cl-, and Br-substituted derivatives, were successfully reduced to their corresponding azobenzene products without any observable dehalogenation, affording high selectivity (**3b–3f**). Furthermore, substrates with para-substituents, whether electron-deficient (**3g–3i**) or electron-donating (**3j** and **3k**), also underwent smooth conversion to azobenzenes with similarly high selectivity. These results underscore the robustness and functional group tolerance of the Au@Δ_2R_6-**Hp** system.

The catalytic performance was further examined with substrates featuring different degrees of steric hindrance. For Cl-substituted nitroarenes, a general selectivity trend of *para* ≈

Table 2 Substrate scope of nitroarenes[a]

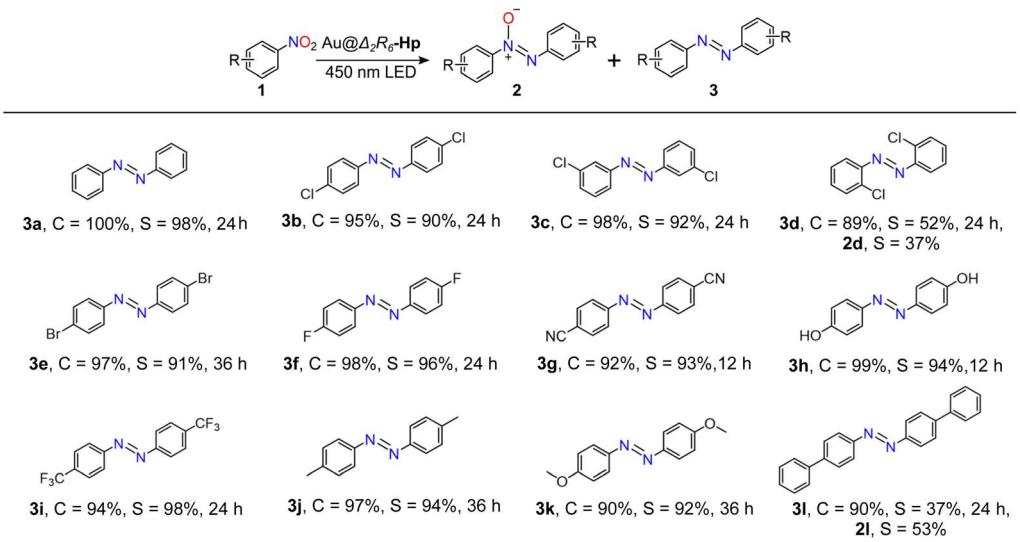

[a] Reaction conditions: Au@Δ_2R_6-**Hp** (1 mol%), 0.1 mmol of substrate **1**, 2 mL of IPA, 0.3 M of NaOH, room temperature, Ar atmosphere, 450 nm LED, reaction time of 12 h, 24 h or 36 h. C for conversion, and S for selectivity.

Open Access Article. Published on 23 April 2026. Downloaded on 6/10/2026 5:52:33 AM.
This article is licensed under a Creative Commons Attribution-NonCommercial 3.0 Unported Licence.

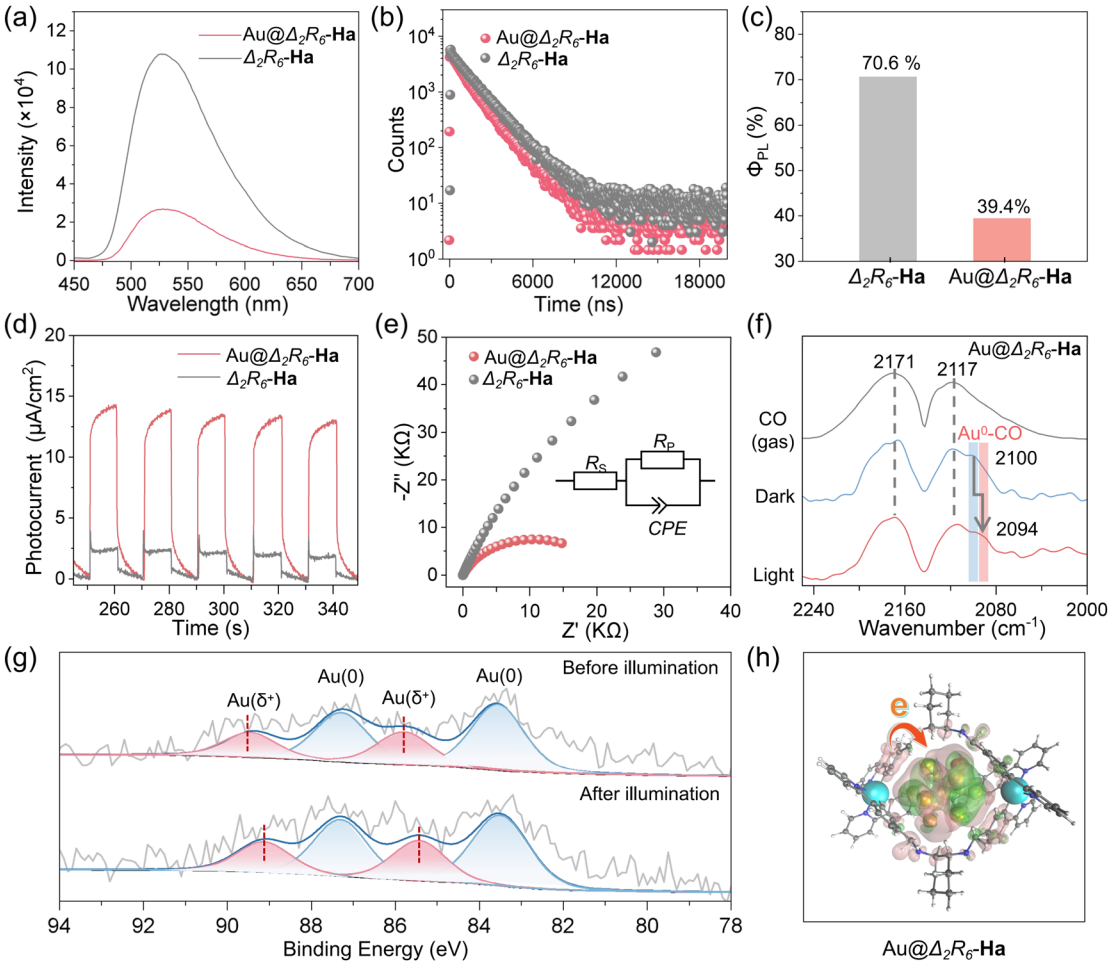

Fig. 3 (a) Luminescent emission spectra, (b) luminescence decay spectra and (c) photoluminescence quantum yields of complexes Δ_2R_6-**Ha** and Au@Δ_2R_6-**Ha** in DMSO (10 μM). (d) Representative photocurrent responses with the interval of 10 s and (e) electrochemical impedance spectroscopies of Δ_2R_6-**Ha** and Au@Δ_2R_6-**Ha** upon irradiation at 450 nm (100 mW cm^{-2}). (f) CO-DRIFTS spectra for gaseous CO (gray curve), Au@Δ_2R_6-**Ha** (blue curve) and Au@Δ_2R_6-**Ha** of the *in situ* irradiation at 450 nm (red curve). (g) *In situ* XPS spectra of Au 4f exhibit the peak shifts, indicating changes in the surface electronic structure after illumination. (h) EDD profiles revealing the electron transfer behavior between cage skeletons and Au–NCs. Color code: Ir atom: cyan; Au atom: yellow; C atom: grey; N atom: blue; H atom: white. Electron density: green and pink color represent the accumulation and reduction of electron density, respectively.

meta > *ortho* was observed (**3b–3d**). In particular, the *ortho*-Cl substituted substrate **1d** exhibited a moderate conversion of 89%, but afforded the desired azobenzene product **3d** in only 52% selectivity, alongside 37% selectivity for the intermediate **2d.** This reduced selectivity likely arises from steric interference near the active site, which impedes the further transformation of **2d** into **3d.** Notably, the catalytic efficiency decreased markedly when bulkier substrates such as biphenyl nitroarenes were employed. For example, substrate **1l** gave significantly lower selectivity toward the final azobenzene product **3l** (only 37%), while the intermediate **2l** dominated with 53% selectivity. This diminished performance is attributed to the increased steric repulsion introduced by the biphenyl group, which likely restricts substrate accommodation within the narrow windows of the cage cavity. Such steric effects highlight the spatial sensitivity of the cage-confined catalytic environment.

PET mechanistic investigation. Under alkaline photocatalytic conditions, the ionized ammonium groups on Au@Δ_2R_6-**Hp** convert to neutral amines, forming Au@Δ_2R_6-**Ha.** We therefore used Au@Δ_2R_6-**Ha** as a model to systematically investigate the synergistic interaction between Au–NCs and the cage host in promoting photocatalytic **NB** reduction. Photophysical characterization revealed that Δ_2R_6-**Ha** displays a broad emission band centered at 529 nm under 405 nm excitation (Fig. 3a), with a long-lived excited state (τ = 1513 ns, Fig. 3b) and a high photoluminescence quantum yield (PLQY = 70.6%, Fig. 3c). These properties resemble those of the commercial Ir(III) complex fac-Ir(ppy)$_3$, validating the cage's intrinsic photoactivity derived from its Ir(III) corners.[52] Upon encapsulation of Au–NCs, however, the emission intensity was significantly quenched by approximately 4-fold, suggesting the occurrence of a PET process. This hypothesis was supported by a shortened excited-state lifetime (τ = 1211 ns) and reduced PLQY (Φ_{PL} = 39.4%) observed for Au@Δ_2R_6-**Ha** (Fig. 3b and c). Furthermore, transient photocurrent measurements under 450 nm LED illumination revealed a 6-fold enhancement in

© 2026 The Author(s). Published by the Royal Society of Chemistry

Open Access Article. Published on 23 April 2026. Downloaded on 6/10/2026 5:52:33 AM. This article is licensed under a Creative Commons Attribution-NonCommercial 3.0 Unported Licence.

current response (Fig. 3d). Electrochemical impedance spectroscopy (EIS) showed a smaller Nyquist semicircle compared to Δ_2R_6-**Ha** alone (Fig. 3e), confirming improved charge separation and faster electron transport within the Au@Δ_2R_6-**Ha**.

To further probe the surface electronic environment of Au–NCs, diffuse reflectance infrared Fourier transform spectroscopy (DRIFTS) was performed using CO as a probe molecule. As shown in Fig. 3f, two vibrational bands at 2171 cm^{-1} and 2117 cm^{-1} were observed after CO adsorption, characteristic of physisorbed CO on Au surfaces.[53] After argon purging, a new band at 2100 cm^{-1} emerged, attributed to CO binding on neutral Au^0 sites.[54] Upon *in situ* 450 nm LED irradiation, this band red-shifted by 6 cm^{-1} to 2094 cm^{-1}, indicating increased electron density on Au due to light-induced electron transfer. Given that CO adsorption frequencies inversely correlate with metal electron density, this shift suggests photoexcitation leads to electron accumulation on the Au surface.[55] In agreement, X-ray photoelectron spectroscopy (XPS) analysis revealed a 0.5 eV shift in the binding energies of $Au^{\delta+}$ peaks after visible light irradiation (from 89.6/85.9 eV to 89.1/85.4 eV; Fig. 3g). This shift further corroborates light-driven electron enrichment at Au–NCs.[1] As shown in Fig. 3h, electron density distribution (EDD) analysis showed that photoexcitation causes significant electron redistribution: electron density accumulates around the encapsulated Au–NCs (green regions) while depleting from the cage skeleton (pink regions).[36] This spatial charge separation confirms the directionality of PET from the Ir-based cage to the Au–NCs. These experimental results collectively demonstrate that the cage's ability to donate electrons to the encapsulated Au–NCs under light irradiation enables the creation of electron-enriched catalytic centers for efficient substrate activation.

Substrate-sieving mechanistic investigation. Building upon the photocatalytic insights, we next carried out time-dependent monitoring experiments to elucidate the kinetics of **NB** reduction. Interestingly, a distinct stepwise reaction pathway emerged (Fig. 4a and S62). In the initial stage (Stage I: 0–10 h), **NB** was gradually consumed, yielding 90% selectivity for **AOB**

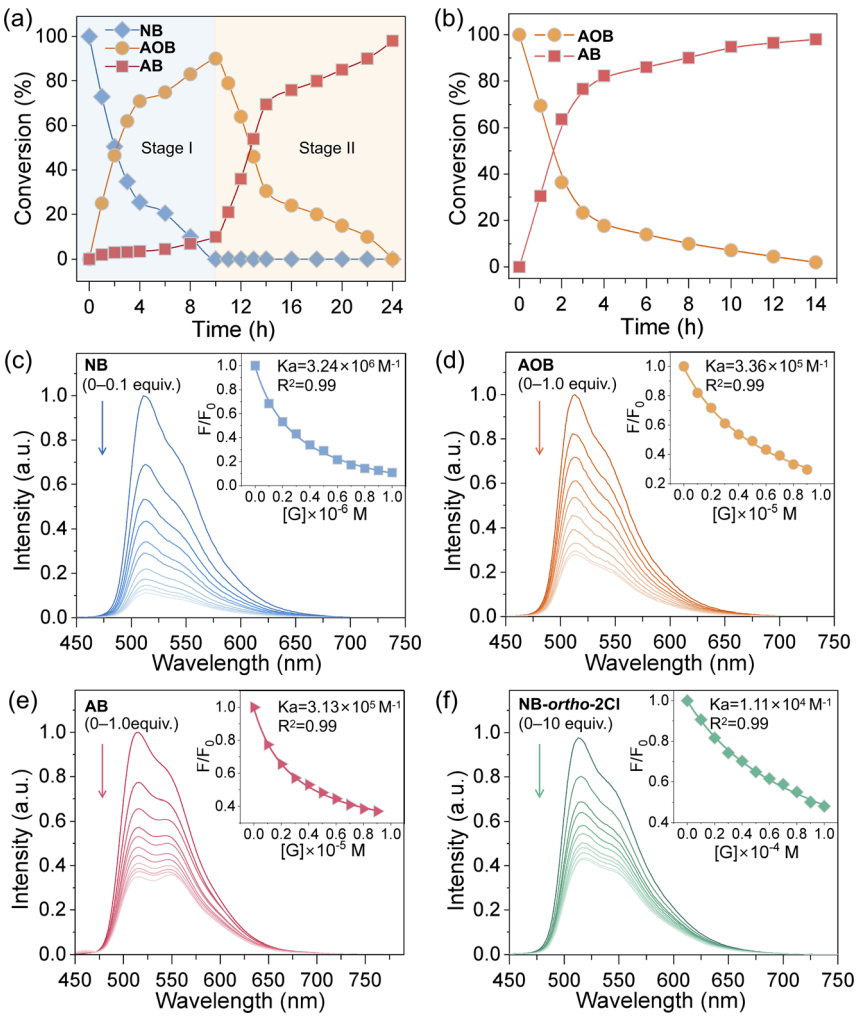

Fig. 4 Kinetic variation of the (a) **NB** and (b) **AOB** reduction catalyzed by Au@Δ_2R_6-**Ha**. The fluorescence quenching of Au@Δ_2R_6-**Ha** (1.0×10^{-5} M) titrated with (c) **NB** (0–0.1 equiv.), (d) **AOB** (0–1.0 equiv.), (e) **AB** (0–1.0 equiv.) and (f) **NB**-*ortho*-**2Cl** (0–10 equiv.) in IPA. Insert: the nonlinear fitting of the titration curves; F_0 and F are the emission intensity in the absence and presence of substrate, respectively; (G) is the concentration of the substrate, K_a is the association constant.

Open Access Article. Published on 23 April 2026. Downloaded on 6/10/2026 5:52:33 AM. This article is licensed under a Creative Commons Attribution-NonCommercial 3.0 Unported Licence.

and 10% for **AB** when **NB** was fully depleted at 10 h. In the subsequent stage (Stage II: >10 h), **AOB** rapidly converted to **AB**, increasing **AB** selectivity to 98%. Given that **AOB** serves as the intermediate, this two-stage behavior implies competitive adsorption between **NB** and **AOB** at the active sites of Au–NCs, where **NB** preferentially binds, thereby retarding **AOB** reduction. This stepwise reaction is supported by the kinetic analysis. A rate constant of $k = 0.091\ M^{-1}\ h^{-1}$ was obtained during the initial 0–4 h of **NB** reduction (Fig. S64a). After complete depletion of **NB** (10–14 h), **AOB** reduction proceeded with $k = 0.278\ h^{-1}$ (Fig. S64b). When **AOB** was used as the sole substrate (Fig. S63), it exhibited a similar kinetic profile (0–4 h) to the **AOB**-to-**AB** conversion stage after **NB** depletion, but with a higher rate constant of $k = 0.455\ h^{-1}$ (Fig. 4b and S64c). Moreover, the initial rate of **NB** reduction showed a second-order dependence on **NB** concentration, supporting a mechanism involving two **NB** molecules in the rate-determining step (Fig. S65). The monitoring procedures were also conducted on the Au/Δ_2R_6-**Ha** catalyst (Fig. S66). With prolonged reaction time, **NB** was consumed while **AOB**, **AB**, and **AN** accumulated progressively with poor selectivity (Fig. S67). The observation that the near complete conversion of **NB** at 24 h yielded only 29% selectivity for **AB** is attributed to the large gold nanoparticles, which non-selectively activated all intermediates and compromised the substrate sieving effect. These results collectively demonstrate that the confined microenvironment of Au@Δ_2R_6-**Ha** allows precise modulation of multistep reduction selectivity by favoring substrate discrimination.

To probe the molecular basis of this selective reduction, we hypothesized that substrate binding affinities, modulated by the metallocage's sterically defined windows, determine access to the Au–NCs catalytic surface. Luminescence titration studies revealed a clear affinity hierarchy: **NB** exhibited the strongest binding with a high association constant ($K_{NB} = 3.24 \times 10^6\ M^{-1}$) and achieved saturation at 10 nM (Fig. 4c). In contrast, **AOB** and **AB** required 10-fold higher concentrations to reach saturation, correlating with their significantly weaker binding constants ($K_{AOB} = 3.36 \times 10^5\ M^{-1}$; $K_{AB} = 3.13 \times 10^5\ M^{-1}$) (Fig. 4d and e). Structural analysis of the cage suggests that its two bent DACH ligands and parallel ppy walls create a confined pocket with rhombic portal-like entrances, which can sieve substrates by steric exclusion. This structure explains why planar but bulky substrates like **AB** and **AOB** are likely to reside at the outer edge of the pocket due to steric hindrance, whereas

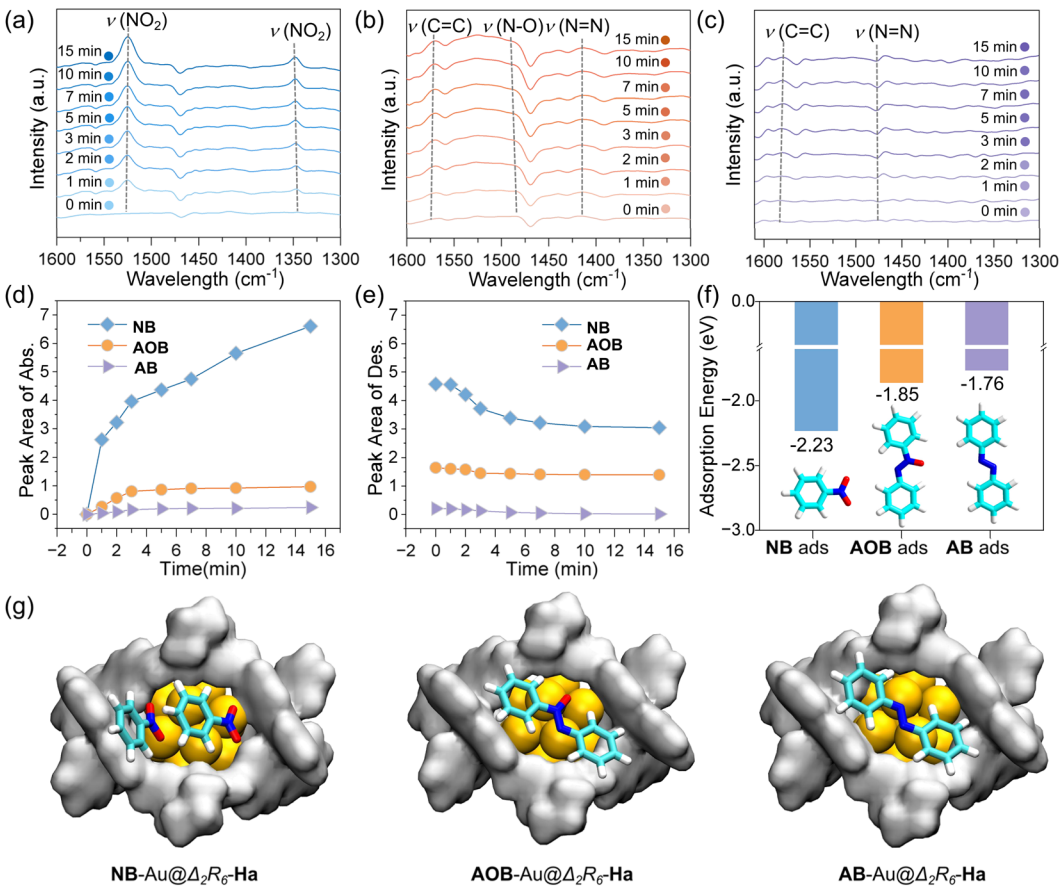

Fig. 5 Time-dependent DRIFTS adsorption of **NB** (a), **AOB** (b) and **AB** (c) on Au@Δ_2R_6-**Ha** (d) the time-dependent adsorption kinetics of **NB**, **AOB** and **AB** on Au@Δ_2R_6-**Ha**, as monitored by peak area evolution (e) the time-dependent desorption kinetics of **NB**, **AOB** and **AB** on Au@Δ_2R_6-**Ha**, as monitored by peak area evolution. Peak areas: the difference between the integral of the peak areas and the integral of the initial peak areas. (f) Adsorption energies of **NB**, **AOB** and **AB** adsorptions on Au@Δ_2R_6-**Ha** by DFT simulations. (g) Models showing the microenvironment of **NB**, **AOB** and **AB** absorption on Au@Δ_2R_6-**Ha**.

© 2026 The Author(s). Published by the Royal Society of Chemistry

Open Access Article. Published on 23 April 2026. Downloaded on 6/10/2026 5:52:33 AM. This article is licensed under a Creative Commons Attribution-NonCommercial 3.0 Unported Licence.

compact **NB** can penetrate deeper for more efficient interactions. This steric exclusion mechanism was further corroborated by luminescence quenching assays using **NB** derivatives with increased bulk. For instance, ortho-chlorinated **NB** (**NB-*ortho*-2Cl**, **1d**) and biphenyl-type **NB** (**NB-2Phen**, **1l**) exhibited drastically reduced binding affinities ($K_a \approx 10^4\ M^{-1}$), two orders of magnitude lower than **NB** (Fig. 4f and S68a), which is consistent with their lower reduction reactivity. Consequently, the Stern–Volmer plots (Fig. S68b and c) confirmed that the interaction with **NB** was one to two orders of magnitude stronger than that with the other compounds (**AOB**, **AB**, **NB-*ortho*-2Cl** and **NB-2Phen**), demonstrating unequivocally that increased steric bulk hinders effective binding.

To validate the spatial confinement mechanism, we employed DRIFTS to monitor substrate adsorption dynamics. **NB** showed strong N=O vibrational bands at ~1348 and ~1525 cm^{-1}, with intensities increasing continuously over 15 minutes (Fig. 5a), confirming strong adsorption *via* its nitro group, while the benzene ring remained non-interacting.[36] In contrast, **AOB** exhibited only weak peaks for C=C, N–O, and N=N bonds (Fig. 5b), likely due to steric repulsion at the cage windows.[56] **AB** showed even weaker adsorption, with minimal spectral changes (Fig. 5c), and faster equilibrium was reached for both **AOB** and **AB** within 3 minutes, compared to over 15 minutes for **NB** (Fig. 5d). Desorption studies further revealed stronger retention of **NB** (10 min to reach equilibrium) *versus* **AOB**/**AB** (5 min), reinforcing the idea of preferential **NB** binding and rapid **AB** release (Fig. 5e and S69). To match the cage cavity dimensions and the experimentally observed cluster size (~0.73 nm), DFT calculations were performed using an icosahedral Au_{13} cluster (Fig. S71 and S72). As shown in Fig. 5g, **NB**s preferentially adsorb *via* their nitro groups in a vertical orientation within the pocket, achieving the strongest adsorption energy (−2.23 eV, Fig. 5f), while the bulkier **AOB** and **AB** adopt parallel orientations and exhibit significantly weaker adsorption energies (−1.85 eV, −1.76 eV). These findings confirm that the rhombic windows enable substrate sieving by favoring **NB** adsorption and **AB** desorption. Further DFT analysis revealed that **NB** reduction to **AB** proceeds with favorable stepwise energetics (Fig. S73), while the over-reduction of **AB** to 2**AN** faces a high activation barrier (3.62 eV), rendering it thermodynamically disfavored. Consequently, the spatially confined Au@Δ_2R_6-**Ha** system not only modulates adsorption and catalytic stages but also ensures product selectivity by blocking excessive hydrogenation.

Conclusions

In summary, by confining ultrasmall Au nanoclusters within a photoactive Ir(III)-based ionic cage, the complete nitrobenzene-to-azobenzene conversion with >98% selectivity was achieved under 450 nm LED irradiation at room temperature *via* an interesting stepwise pathway involving azoxybenzene intermediates. The system operates through a synergistic dual-regulation mechanism by integrating the light-harvesting ability of the Ir(III) metallocage with the catalytic function of the Au nanoclusters: (1) PET from the excited cage to the embedded Au nanoclusters generates electron-rich active sites, facilitating substrate activation; (2) the size-selective windows of the cage provide substrate-sieving functionality, which governs reactant adsorption and ensures high chemoselectivity. This work exemplifies how the fusion of photocatalytic activity and molecular recognition within a single supramolecular cage-nanocluster platform can yield catalysts with tailored activity and selectivity. Furthermore, extending this design concept to other redox-active metal clusters and functional cages presents a promising strategy for the simultaneous stabilization, microenvironment engineering, and catalytic selectivity tuning of nanoclusters.

Author contributions

Zhuolin Shi performed molecular synthesis and experiments, analyzed the data, conducted the computational studies, and wrote the original draft. Fengyang Yu contributed to spherical aberration-corrected HAADF-STEM measurements and data analysis. Jinguo Wu assisted with molecular synthesis. Wenjing Jiang conducted XPS measurements. Rong Zhang performed HR-Q-TOF-MS measurements. Jianwei Wei assisted with kinetic analysis. Yongai Yu, Fengyang Yu, Hanshu Li, Xing Zhao, Yiwei Liu, and Cheng He contributed to scientific discussions and manuscript review and editing. Xuezhao Li conceived and designed the project, supervised the study, contributed to data analysis, acquired funding, contributed to the original draft, and revised the manuscript.

Conflicts of interest

The authors declare no conflict of interest.

Data availability

The data generated in this study are provided in the article, supplementary information (SI) and from corresponding author(s) upon request. Supplementary information: synthesis, NMR and MS characterizations, photophysical measurements, photocatalytic experiments, and DFT. See DOI: https://doi.org/10.1039/d6sc01364c.

Acknowledgements

This research work was financially supported by the National Natural Science Foundation of China (grant nos. 22477014, 22171033 and 22571032), the Fundamental Research Funds for the Central Universities [DUT25Z2504], and the Liaoning Provincial Science and Technology Plan Joint Program (Natural Science Foundation-General Program, 2024-MSLH-070). We thank Dr Cai Rui in Instrumental Analysis Center of Dalian University of Technology for assistance with photoluminescence spectroscopy.

Open Access Article. Published on 23 April 2026. Downloaded on 6/10/2026 5:52:33 AM. This article is licensed under a Creative Commons Attribution-NonCommercial 3.0 Unported Licence.

Notes and references

1 J. Z. Zhang, Y. B. Zhang, H. L. Chai, H. L. Luo, C. X. Du, R. W. Huang and S. Q. Zang, Selectivity Modulation of Multistep Reduction Reactions by Gold Nanoclusters, *Angew. Chem., Int. Ed.*, 2025, **64**, e202413418.

2 X. Ma, Z. Zhang, D. Zhao, J. Peng, S. Xing, R. Huang, S. Li, N. Ma and Y. Liu, Spatially Confined Construction of Ultrasmall Pd Clusters Within Nitro-Bonded Covalent Organic Frameworks for Efficient Alkyne Semihydrogenation, *Small*, 2025, **21**, 2410416.

3 H. Kang, J. T. Buchman, R. S. Rodriguez, H. L. Ring, J. He, K. C. Bantz and C. L. Haynes, Stabilization of Silver and Gold Nanoparticles: Preservation and Improvement of Plasmonic Functionalities, *Chem. Rev.*, 2019, **119**, 664–699.

4 E. L. Albright, T. I. Levchenko, V. K. Kulkarni, A. I. Sullivan, J. F. DeJesus, S. Malola, S. Takano, M. Nambo, K. Stamplecoskie, H. Häkkinen, T. Tsukuda and C. M. Crudden, N-Heterocyclic Carbene-Stabilized Atomically Precise Metal Nanoclusters, *J. Am. Chem. Soc.*, 2024, **146**, 5759–5780.

5 K. Ueda, R. Saito, K. Iseri, S. Sekiya, M. Nakamura and K. Isozaki, Accelerated Catalysis of Atomically Precise Thiolate-Protected Gold Nanoclusters by Supramolecular Ligand Engineering, *ACS Catal.*, 2025, **15**, 12260–12268.

6 Y. Zhong, P. Liao, P. Jiang, Y. Zhang, J. Kang, S. Xie, R. Feng, Y. Fan, Q. Liu and G. Li, Ionic-Fence Effect in Au Nanoparticle-Loaded UiO-66 Metal–Organic Frameworks for Highly Chemoselective Hydrogenation, *Angew. Chem., Int. Ed.*, 2025, **64**, e202501821.

7 C. He, Q. J. Wu, M. J. Mao, Y. H. Zou, B. T. Liu, Y. B. Huang and R. Cao, Multifunctional Gold Nanoparticles @Imidazolium-Based Cationic Covalent Triazine Frameworks for Efficient Tandem Reactions, *CCS Chem.*, 2020, **3**, 2368–2380.

8 R. W. Y. Man, C. H. Li, M. W. A. MacLean, O. V. Zenkina, M. T. Zamora, L. N. Saunders, A. Rousina-Webb, M. Nambo and C. M. Crudden, Ultrastable Gold Nanoparticles Modified by Bidentate N-Heterocyclic Carbene Ligands, *J. Am. Chem. Soc.*, 2018, **140**, 1576–1579.

9 L. M. Cao, J. Zhang, X. F. Zhang and C. T. He, Confinement Synthesis in Porous Molecule-based Materials: A New Opportunity for Ultrafine Nanostructures, *Chem. Sci.*, 2022, **13**, 1569–1593.

10 Q. Fu and X. Bao, Confined Microenvironment for Catalysis Control, *Nat. Catal.*, 2019, **2**, 834–836.

11 E. L. Bell, W. Finnigan, S. P. France, A. P. Green, M. A. Hayes, L. J. Hepworth, S. L. Lovelock, H. Niikura, S. Osuna, E. Romero, K. S. Ryan, N. J. Turner and S. L. Flitsch, Biocatalysis, *Nat. Rev. Methods Primers*, 2021, **1**, 46.

12 L. Lancaster, W. Abdallah, S. Banta and I. Wheeldon, Engineering Enzyme Microenvironments for Enhanced Biocatalysis, *Chem. Soc. Rev.*, 2018, **47**, 5177–5186.

13 H. Takezawa and M. Fujita, Molecular Confinement Effects by Self-Assembled Coordination Cages, *Bull. Chem. Soc. Jpn.*, 2021, **94**, 2351–2369.

14 J. Meeuwissen and J. N. H. Reek, Supramolecular catalysis beyond enzyme mimics, *Nat. Chem.*, 2010, **2**, 615–621.

15 Y. L. Lu, Y. P. Wang, K. Wu, M. Pan and C. Y. Su, Activating Metal–Organic Cages by Incorporating Functional $M(ImPhen)_3$ Metalloligands: From Structural Design to Applications, *Acc. Chem. Res.*, 2024, **57**, 3277–3291.

16 R. McCaffrey, H. Long, Y. Jin, A. Sanders, W. Park and W. Zhang, Template Synthesis of Gold Nanoparticles with an Organic Molecular Cage, *J. Am. Chem. Soc.*, 2014, **136**, 1782–1785.

17 Y. Zhang, J. Zhou, K. Luo, W. Zhou, F. Wang, J. Li and Q. He, Ferritin-Inspired Encapsulation and Stabilization of Gold Nanoclusters for High-Performance Photothermal Conversion, *Angew. Chem., Int. Ed.*, 2025, **64**, e202500058.

18 X. X. Gou, T. Liu, Y. Y. Wang and Y. F. Han, Ultrastable and Highly Catalytically Active N-Heterocyclic-Carbene-Stabilized Gold Nanoparticles in Confined Spaces, *Angew. Chem., Int. Ed.*, 2020, **59**, 16683–16689.

19 M. Nihei, H. Ida, T. Nibe, A. M. P. Moeljadi, Q. T. Trinh, H. Hirao, M. Ishizaki, M. Kurihara, T. Shiga and H. Oshio, Ferrihydrite Particle Encapsulated within a Molecular Organic Cage, *J. Am. Chem. Soc.*, 2018, **140**, 17753–17759.

20 Y. Fang, J. Li, T. Togo, F. Jin, Z. Xiao, L. Liu, H. Drake, X. Lian and H. C. Zhou, Ultra-Small Face-Centered-Cubic Ru Nanoparticles Confined within a Porous Coordination Cage for Dehydrogenation, *Chem*, 2018, **4**, 555–563.

21 S. Y. Zhang, Z. Kochovski, H.-C. Lee, Y. Lu, H. Zhang, J. Zhang, J. K. Sun and J. Yuan, Ionic Organic Cage-encapsulating Phase-transferable Metal Clusters, *Chem. Sci.*, 2019, **10**, 1450–1456.

22 C. Wang, F. Sun, G. He, H. Zhao, L. Tian, Y. Cheng and G. Li, Noble Metal Nanoparticles Meet Molecular Cages: A Tale of Integration and Synergy, *Curr. Opin. Colloid Interface Sci.*, 2023, **63**, 101660.

23 S. L. Hou, J. Dong, Z. H. Zhu, L. C. Geng, Y. Ma and B. Zhao, Size-Tunable Ultrafine Pt Nanoparticles in Soluble Metal–Organic Cages: Displaying Highly Stereoselective Hydrogenation of α-Pinene, *Chem. Mater.*, 2020, **32**, 7063–7069.

24 Y. Fang, J. Li, T. Togo, F. Jin, Z. Xiao, L. Liu, H. Drake, X. Lian and H. C. Zhou, Ultra-Small Face-Centered-Cubic Ru Nanoparticles Confined within a Porous Coordination Cage for Dehydrogenation, *Chem*, 2018, **4**, 555–563.

25 L. L. Metz, R. Ham, E. O. Bobylev, K. J. H. Brouwer, A. van Blaaderen, R. C. J. van de Poll, V. R. Drozhzhin, E. J. M. Hensen and J. N. H. Reek, $M_{12}L_{24}$ Nanospheres as Supramolecular Templates for the Controlled Synthesis of Ir-Nanoclusters and Their Use in the Chemo-selective Hydrogenation of Nitro Styrene, *Chem. Sci.*, 2024, **15**, 20022–20029.

26 L. L. Metz, E. O. Bobylev, R. C. J. vandePoll, E. J. M. Hensen, I. Hoogsteder, W. Albrecht and J. N. H. Reek, Supramolecular Preorganization Rhodium and Iridium Metal Complexes Within $M_{12}L_{24}$ Self-Assembled Nanospheres for the Confined Synthesis Rh/Ir Alloyed Nanoparticles, *ChemCatChem*, 2025, **17**, e202401161.

© 2026 The Author(s). Published by the Royal Society of Chemistry

Open Access Article. Published on 23 April 2026. Downloaded on 6/10/2026 5:52:33 AM. This article is licensed under a Creative Commons Attribution-NonCommercial 3.0 Unported Licence.

27 X. Hang, S. Wang, H. Pang and Q. Xu, A Coordination Cage Hosting Ultrafine and Highly Catalytically Active Gold Nanoparticles, *Chem. Sci.*, 2022, **13**, 461–468.
28 Y. J. Du, J. H. Zhou, L. X. Tan, S. H. Liu, K. Zhao, Z. M. Gao and J. K. Sun, Porous Organic Cage Nanostructures for Construction of Complex Sequential Reaction Networks, *ACS Appl. Nano Mater.*, 2022, **5**, 7974–7982.
29 Y. Fang, Z. Xiao, J. Li, C. Lollar, L. Liu, X. Lian, S. Yuan, S. Banerjee, P. Zhang and H. C. Zhou, Formation of a Highly Reactive Cobalt Nanocluster Crystal within a Highly Negatively Charged Porous Coordination Cage, *Angew. Chem., Int. Ed.*, 2018, **57**, 5283–5287.
30 X. Yang, J. K. Sun, M. Kitta, H. Pang and Q. Xu, Encapsulating Highly Catalytically Active Metal Nanoclusters Inside Porous Organic Cages, *Nat. Catal.*, 2018, **1**, 214–220.
31 J. K. Sun, W. W. Zhan, T. Akita and Q. Xu, Toward Homogenization of Heterogeneous Metal Nanoparticle Catalysts with Enhanced Catalytic Performance: Soluble Porous Organic Cage as a Stabilizer and Homogenizer, *J. Am. Chem. Soc.*, 2015, **137**, 7063–7066.
32 M. Zhang, R. Liu, Z. He, L. Wang, X. Zhang and G. Li, Large Triazine Organic Cage Encapsulating Pd Nanoclusters for Selective Hydrogenation of Alkynes, *ACS Catal.*, 2025, **15**, 12247–12259.
33 B. Mondal and P. S. Mukherjee, Cage Encapsulated Gold Nanoparticles as Heterogeneous Photocatalyst for Facile and Selective Reduction of Nitroarenes to Azo Compounds, *J. Am. Chem. Soc.*, 2018, **140**, 12592–12601.
34 B. Mondal, K. Acharyya, P. Howlader and P. S. Mukherjee, Molecular Cage Impregnated Palladium Nanoparticles: Efficient, Additive-Free Heterogeneous Catalysts for Cyanation of Aryl Halides, *J. Am. Chem. Soc.*, 2016, **138**, 1709–1716.
35 M. Raynal, P. Ballester, A. Vidal-Ferran and P. W. N. M. van Leeuwen, Supramolecular Catalysis. Part 2: Artificial Enzyme Mimics, *Chem. Soc. Rev.*, 2014, **43**, 1734–1787.
36 S. Ren, L. Tan, J. H. Zhou, J. Sun, P. Zhang, X. Cao, Y. H. Zhang and J. K. Sun, Eco-Friendly Encapsulation of Metal Clusters in Porous Organic Cages for Engineerable Microenvironment and Enhanced Catalysis, *CCS Chem.*, 2024, **6**, 2186–2197.
37 X. Zhou, Z. Wang, Z. N. Chen and Y. Yang, Phosphine-Built-In Porous Organic Cage Supported Ultrafine Pd Nanoclusters Enable Highly Efficient and Regioselective Hydrogenation of Epoxides, *CCS Chem.*, 2024, **6**, 2476–2488.
38 K. E. Jelfs, X. Wu, M. Schmidtmann, J. T. A. Jones, J. E. Warren, D. J. Adams and A. I. Cooper, Large Self-Assembled Chiral Organic Cages: Synthesis, Structure, and Shape Persistence, *Angew. Chem., Int. Ed.*, 2011, **50**, 10653–10656.
39 M. Liu, M. A. Little, K. E. Jelfs, J. T. A. Jones, M. Schmidtmann, S. Y. Chong, T. Hasell and A. I. Cooper, Acid- and Base-Stable Porous Organic Cages: Shape Persistence and pH Stability via Post-synthetic "Tying" of a Flexible Amine Cage, *J. Am. Chem. Soc.*, 2014, **136**, 7583–7586.
40 M. Wilms, L. V. Melendez, R. J. Hudson, C. R. Hall, S. P. Ratnayake, T. Smith, E. D. Gaspera, G. Bryant, T. U. Connell and D. E. Gómez, Photoinitiated Energy Transfer in Porous-Cage-Stabilised Silver Nanoparticles, *Angew. Chem., Int. Ed.*, 2023, **62**, e202303501.
41 N. Sun, C. Wang, H. Wang, L. Yang, P. Jin, W. Zhang and J. Jiang, Multifunctional Tubular Organic Cage-Supported Ultrafine Palladium Nanoparticles for Sequential Catalysis, *Angew. Chem., Int. Ed.*, 2019, **58**, 18011–18016.
42 J. Wu, X. Li, P. Wu, Z. Shi, L. Chen, R. Zhang, C. He and C. Duan, Engineering Homochiral Dinuclear Ir(III)-Metallohelix-Based Porous Molecular Crystals for Atropisomer Enantioseparation, *Chem. Mater.*, 2022, **34**, 4471–4478.
43 Z. Shi, Y. Wang, R. Zhang, H. Li, R. Cai, J. Wu, X. Wang, H. Li, X. Li and C. He, Confining Cu(I) ions within an Ir(III)-based Twin-cavity Cage for Photo-triggered Dioxygen Activation toward C(sp^3)–H Oxidation, *Inorg. Chem. Front.*, 2025, **12**, 2515–2523.
44 J. Chen, Y. L. Lu, Y. Huang, F. Zhang, H. Ye, Y.-H. Huang, X.-D. Zhang, Z. Jiao and C. Y. Su, Asymmetric Cascade Photocycloaddition-Acyloin Rearrangement Enabled by Cage-Confined Visible-Light Catalysis, *J. Am. Chem. Soc.*, 2025, **147**, 13008–13016.
45 S. Zhou, W. Cao, L. Shang, Y. Zhao, X. Xiong, J. Sun, T. Zhang and J. Yuan, Facilitating Alkaline Hydrogen Evolution Kinetics via Interfacial Modulation of Hydrogen-bond Networks by Porous Amine Cages, *Nat. Commun.*, 2025, **16**, 1849.
46 K. Esumi, A. Suzuki, N. Aihara, K. Usui and K. Torigoe, Preparation of Gold Colloids with UV Irradiation Using Dendrimers as Stabilizer, *Langmuir*, 1998, **14**, 3157–3159.
47 E. Merino, Synthesis of Azobenzenes: the Coloured Pieces of Molecular Materials, *Chem. Soc. Rev.*, 2011, **40**, 3835–3853.
48 K. Hüll, J. Morstein and D. Trauner, In Vivo Photopharmacology, *Chem. Rev.*, 2018, **118**, 10710–10747.
49 A. Corma, P. Concepción and P. Serna, A Different Reaction Pathway for the Reduction of Aromatic Nitro Compounds on Gold Catalysts, *Angew. Chem., Int. Ed.*, 2007, **46**, 7266–7269.
50 H. Zhu, X. Ke, X. Yang, S. Sarina and H. Liu, Reduction of Nitroaromatic Compounds on Supported Gold Nanoparticles by Visible and Ultraviolet Light, *Angew. Chem., Int. Ed.*, 2010, **49**, 9657–9661.
51 Y. Dai, C. Li, Y. Shen, T. Lim, J. Xu, Y. Li, H. Niemantsverdriet, F. Besenbacher, N. Lock and R. Su, Light-tuned Selective Photosynthesis of Azo- and Azoxy-aromatics Using Graphitic C_3N_4, *Nat. Commun.*, 2018, **9**, 60–67.
52 A. B. Tamayo, B. D. Alleyne, P. I. Djurovich, S. Lamansky, I. Tsyba, N. N. Ho, R. Bau and M. E. Thompson, Synthesis and Characterization of Facial and Meridional Tris-cyclometalated Iridium(III) Complexes, *J. Am. Chem. Soc.*, 2003, **125**, 7377–7387.
53 B. Wei, X. Liu, Y. Deng, K. Hua, J. Chen, H. Wang and Y. Sun, Efficient and Stable Co/β-Mo_2C Catalyst for Hydroformylation, *ACS Catal.*, 2021, **11**, 14319–14327.

Open Access Article. Published on 23 April 2026. Downloaded on 6/10/2026 5:52:33 AM.
This article is licensed under a Creative Commons Attribution-NonCommercial 3.0 Unported Licence.

54 J. Luo, Y. Liu, Y. Niu, Q. Jiang, R. Huang, B. Zhang and D. Su, Insight into the Chemical Adsorption Properties of CO Molecules Supported on Au or Cu and Hybridized Au–CuO Nanoparticles, *Nanoscale*, 2017, **9**, 15033–15043.

55 H. Wang, X. Liu, W. Yang, G. Mao, Z. Meng, Z. Wu and H.-L. Jiang, Surface-Clean Au_{25} Nanoclusters in Modulated Microenvironment Enabled by Metal–Organic Frameworks for Enhanced Catalysis, *J. Am. Chem. Soc.*, 2022, **144**, 22008–22017.

56 G. Richner, J. A. van Bokhoven, Y. M. Neuhold, M. Makosch, K. Hungerbühler and K. In, Situ Infrared Monitoring of the Solid/liquid Catalyst Interface During the Three-phase Hydrogenation of Nitrobenzene Over Nanosized Au on TiO_2, *Phys. Chem. Chem. Phys.*, 2011, **13**, 12463–12471.

© 2026 The Author(s). Published by the Royal Society of Chemistry